Iceland Liechtenstein Norway grants

uefiscdi
Executive Agency for Higher Education, Research, Development and Innovation Funding

ANNUAL REPORTING

2020

A2.1.1 Advanced tunable imaging designs by PWE, FDTD (SINTEF- P1)

In order to achieve a tunable focal length of the metalenses, the meta-structure is to be embedded in PDMS and lifted off the Si substrate. By stretching the PDMS-embedded metastructure, the focal distance of the lens is changed by the amount $\Delta f = \epsilon_s(2+\epsilon_s)f$, where f is the unstretched focal length and $\epsilon_s = \Delta d/d$ is the strain (i.e. the change in diameter Δd of the lens relative to the unstretched diameter d). New metasurface designs have been made for metastructures embedded in PDMS without substrate, which were optimized with respect to varying periodicities in the range $p \in [0.55\mathrm{\mu m}, 0.85\mathrm{\mu m}]$. Examples are given in Fig.1. Upon the removal of the Si substrate the PDMS layer acts as a waveguide layer owing to the fact that it has a higher index than the surrounding air and that its thickness is comparable to the wavelength (Fig. 1b).

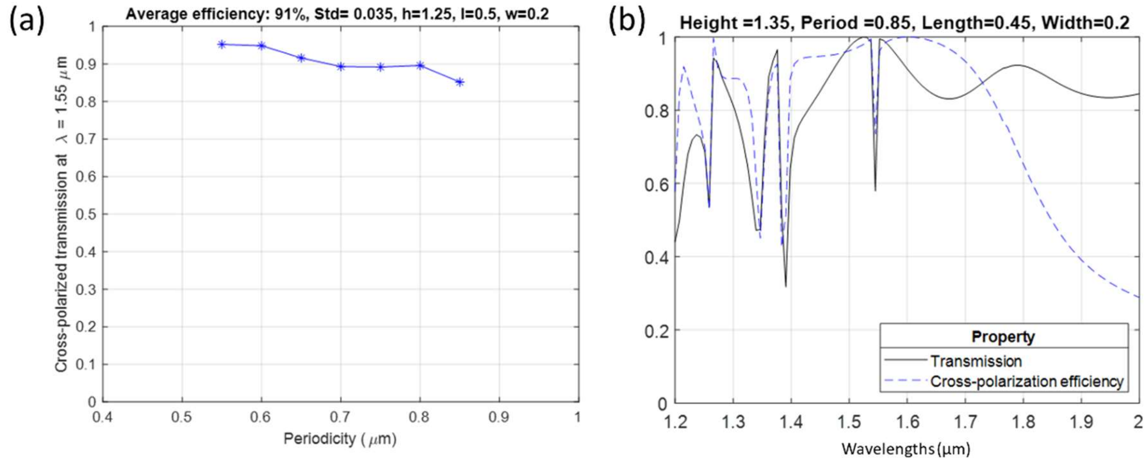

Fig 1: (a) Transmitted cross-polarized field upon changing lattice periodicity. Here the structure gives high and relatively flat transmission as the periodicity is changed between $p \in [0.55\mathrm{\mu m}, 0.85\mathrm{\mu m}]$. (b) Transmitted cross-polarized field for different wavelengths. The presence of Fano-resonances is visible.

P1 have implemented a hologram design technique using the Gerchberg Saxton algorithm in combination with beam propagation using the angular spectrum representation of electromagnetic fields. Currently, among the tested implementation ideas the stretchable lens and aperture configuration is the most promising for high SNR.

Sensor system design. A varifocal lens setup has been designed and thoroughly analysed analytically and initial verification using Zemax simulation software has been conducted. Sketches for components necessary to achieve radial stretching of the metalenses has been made.

A 2.1.2: Advanced tunable imaging designs by COMSOL (P3-partner)

In 2020, P3 have shown, using analytical expressions and numerical simulations in COMSOL, that metalenses that impart a controlled phase difference between cross-polarized circular reflected and transmitted fields can be designed to act also as thermal emitters. In particular, the thermal emissivity of these advanced imaging devices can be tuned by selecting the proper geometry of the metasurface's unit cell.

In the vast majority of cases, metasurfaces are optimized for a desired application: imaging, focusing, generation of twisted light beams, etc. However, there are metasurfaces designed to fulfil more than one task [1]. In particular, P3 have demonstrated that metasurfaces could impart a controllable relative phase between the two orthogonal fields that form the circular polarization basis, and can thus be used to focus an incident electromagnetic field, while acting at the same time as a thermal emitter in the near-infrared spectrum, i.e., having a finite absorption at the working wavelength.

Simulation work (detailed)

- ***Have have investigated two types of metasurfaces that couple the fields of the circular polarization basis***, their defining property being that they can be characterized by a local polarizability tensor with two orthogonal components α_x and α_y . In this case, both analytical and numerical simulations can be performed, with remarkable agreement between them.

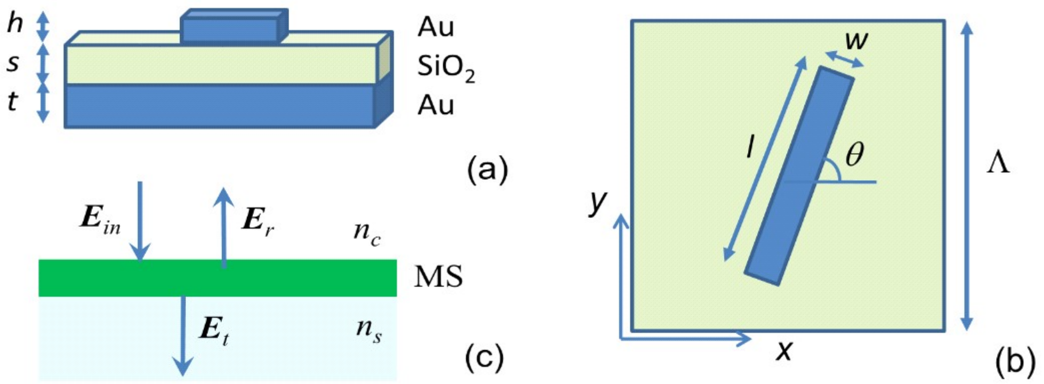

Fig. 2

The unit cell of the metasurface that we consider is represented in Figs. 2(a) and 1(b). It consists of a highly anisotropic metallic meta-atom with height, width and length denoted by *h*, *w*, *l*, respectively, placed over a dielectric substrate with thickness *s* (SiO_2, with refractive index n_s = 1.447), which in turn is situated on top of a continuous metallic layer with thickness *t* much higher than the skin depth (*t* = 0 if the bottom metal layer is not present). The metal is gold. The unit cells are arranged in a square lattice of period Λ, and the meta-atom can rotate in the metasurface plane, denoted as the (*x*,*y*) plane.

- Considering that the equivalent structure of the metasurface, illustrated in Fig. 1(c), consists of a cover layer of refractive index n_c (air, with n_c = 1), the ultrathin metasurface (denoted MS) with a local polarizability tensor with diagonal components α_x and α_y, and a substrate layer with refractive index n_s, the components of the transmitted electromagnetic field, $\boldsymbol{E}_t$, at normal incidence in the circular polarization basis, are related to the respective components of the incoming field, $\boldsymbol{E}_{in}$, incident from the cover.

$$\begin{pmatrix} E_{t,R} \\ E_{t,L} \end{pmatrix} = \frac{2n_c}{n^2+(k_0\alpha_-)^2} \begin{pmatrix} n & ik_0\alpha_- \exp(-i2\theta) \\ ik_0\alpha_- \exp(i2\theta) & n \end{pmatrix} \begin{pmatrix} E_{in,R} \\ E_{in,L} \end{pmatrix} = \begin{pmatrix} A & B \\ C & D \end{pmatrix} \begin{pmatrix} E_{in,R} \\ E_{in,L} \end{pmatrix} \tag{1}$$

In equation (1) the subscripts *R* and *L* stand for right- and left-circular polarizations, respectively, $k_0 = \omega / c = 2\pi / \lambda$, $\alpha_{\pm} = (\alpha_x \pm \alpha_y)/2$, and $n = n_c + n_s - ik_0\alpha_+$. The components of the reflected field can be found using the boundary condition $\boldsymbol{E}_{in} + \boldsymbol{E}_r = \boldsymbol{E}_t$. Equation (1) indicates that a phase difference determined only by the rotation angle θ of the metallic meta-atoms develops between the cross-polarized components, while the co-polarized (transmitted or reflected) wave acquires a constant, θ-independent, phase.

A. Metasurfaces without bottom metallic layer

The structure in Fig. 2, for Λ = 450 nm, *h* = 30 nm, *w* = 80 nm, and *l* = 300 nm, illuminated with linearly polarized light along *x* and *y* axes, can be characterized by diagonal α_x și α_y, components of the polarization tensor of a Lorentzian form:

$$\alpha_{x,y} = \frac{cg_{x,y}\gamma_{x,y}}{\omega^2 - \omega_{x,y}^2 - i\omega_{x,y}\gamma_{x,y}} \tag{2}$$

with *c* the speed of light in vacuum and $\omega_{x,y} = 2\pi c / \lambda_{x,y}$. Indeed, the simulated transmission *T*, reflection *R*, and absorption *A* shown in Figs. 3(a) and 3(b) are in agreement with Lorentzian polarizations if fitted with the parameters g_x = 13, g_y = 1.3, γ_x = 6.8 1013, γ_y = 201012, λ_x = 1.27 μm, and λ_y = 0.6 μm.Then, as can be seen from Fig. 3(c), the *R*, *T* and *A* parameters obtained from (1) with these fitting values and those simulated numerically by COMSOL for an incident infrared left-polarized electric field are in good agreement; in the following all incident fields will be considered left-circularly-polarized.

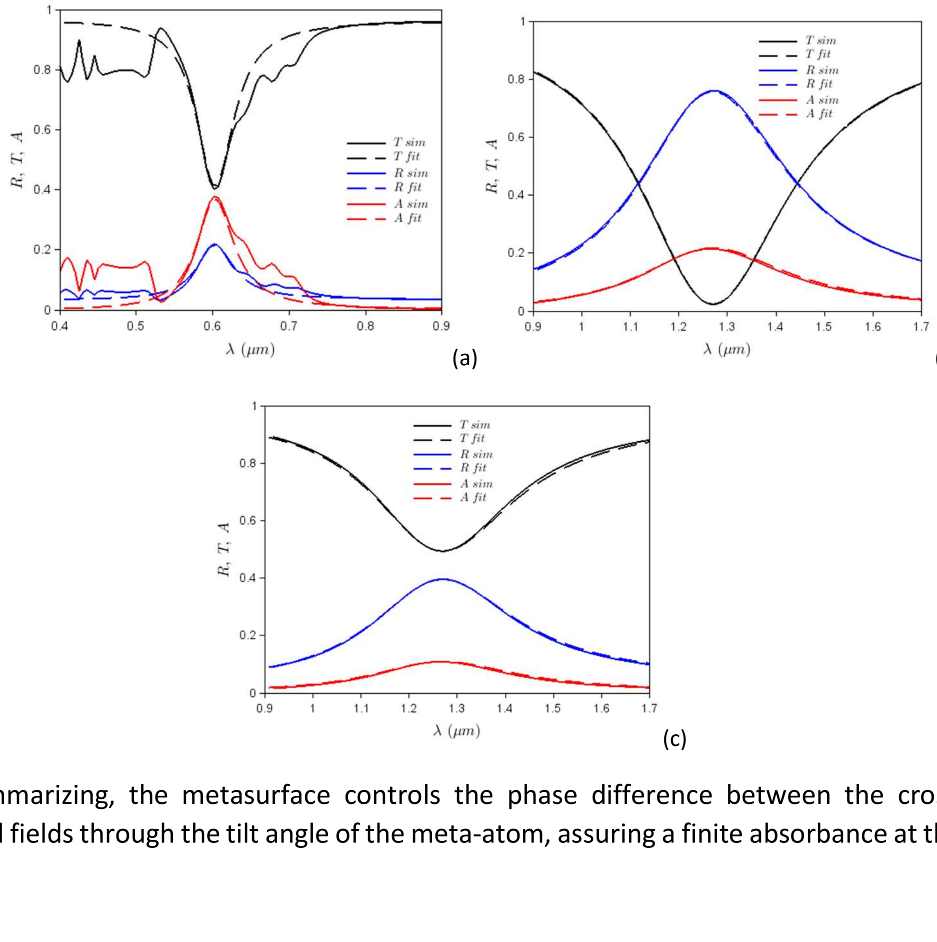

(a) (b) (c) *Fig. 3*

Summarizing, the metasurface controls the phase difference between the cross- and co-polarized fields through the tilt angle of the meta-atom, assuring a finite absorbance at the resonant near-infrared wavelength. The resonant wavelength of the metasurface as well as the absorbance, and reflectance (dashed lines) and transmittance (solid lines) of cross-polarized fields (subscript *cross*) vary smoothly with the parameters of the structure, as can be seen from Figs. 4(a) and 4(b), respectively. The maximum absorbance value increases (and the cross-polarized fields decrease) as the filling/packing density of the unit cell decreases (as *w*, *l* and *h* decrease with respect to the structure with *h* = 30 nm, *w* = 80 nm and *l* = 300 nm); these results are consistent with the findings in [4]. The resonant wavelengths shift to lower values with increasing *h* and *w*, and to higher values as *l* increases. However, although the range of parameters was quite wide, we found that both cross-polarized fields and absorbance remain quite small. Therefore, we have investigated in the following section grounded structures, expecting that, especially the absorbance, increases.

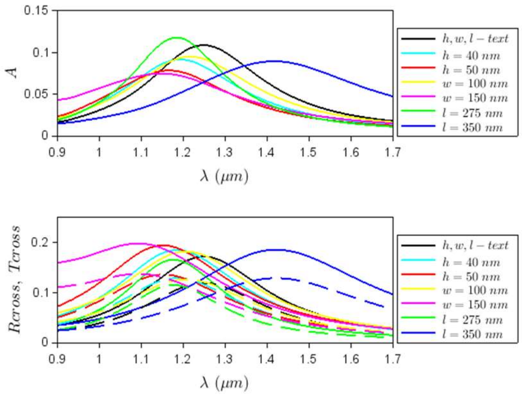

Fig. 4

B. Metasurfaces with bottom metallic layer

Similar simulations have been performed for grounded metasurfaces, with a bottom metallic layer for which COMSOL simulations for $\theta = 0$ and for illumination with linearly polarized light along *x* and *y* axes revealed resonances with complex forms, which could not be fitted by single Lorentzian α_x and α_y polarization tensor components. Nevertheless, the symmetry of meta-atoms assures that the local polarizability tensor has two orthogonal/diagonal components α_x and α_y, such that the form of (1) remains unchanged.

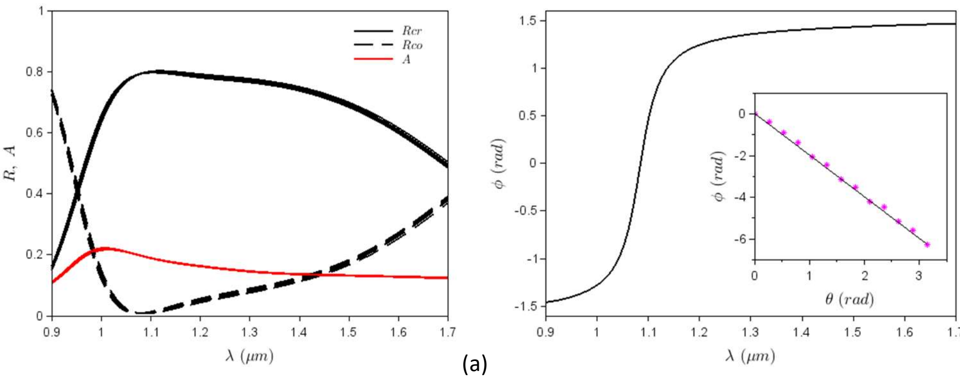

(a) (b)

Fig. 5

This statement is confirmed by Figs. 5, 6 and 7, which illustrate numerical simulation results for similar structures as in the previous section (*h* = 30 nm, *w* = 80 nm and *l* = 300 nm) and thicknesses of the dielectric layer of 200 nm, 150 nm and 100 nm, respectively. In this case no transmitted light exists and, compared to the non-grounded metasurfaces, near the resonant wavelengths in the near-infrared region the absorbance, as well as the cross-polarized reflectance are larger; the absorbance in all cases is about 20%, while the power in the cross-polarized light is about 80% from the incident one at resonance, wavelength at which the co-polarized reflectance is very small. Thus, the metallic bottom layer acts as catalysts for power coupling to the cross-polarized field. In all cases, the phase difference between cross- and co-polarized reflected light is twice the tilt angle θ of the meta-atom.

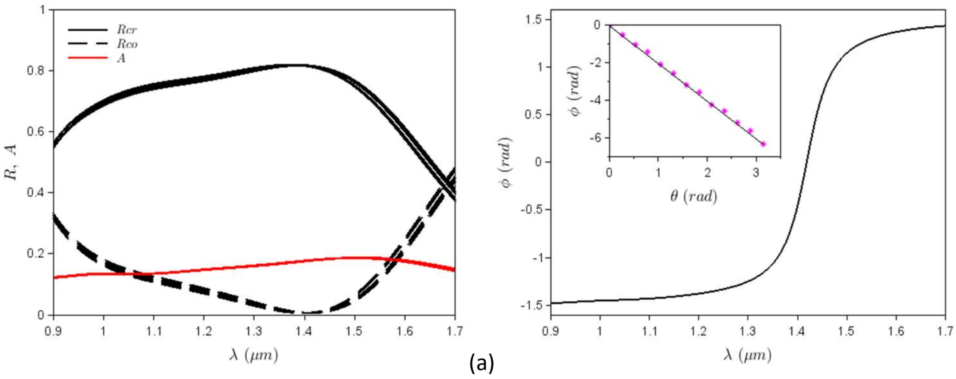

(a) (b)

Fig. 6

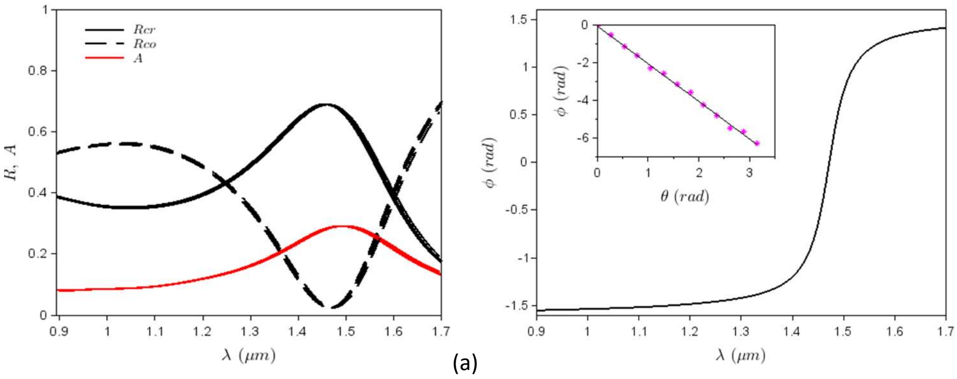

(a) (b)

Fig. 7

Again, by varying the geometric parameters of the meta-atom, we have investigated the variation of absorbance (solid line), reflectance of cross-polarized light (dashed line) and resonant wavelengths (see Fig. 8) for the structure with *s* = 200 nm. The behaviour of these quantities differ from that in non-grounded structures studied before, the most evident difference being the significant change of the shape of cross-polarized reflectance curves over the interval of parameters considered. The maximum *A* value increases as *l* decreases, and *h* and *w* increase, while the resonant wavelengths shift to lower values developing at the same time a sharper resonance with increasing *h* and *w*, and to higher values and broader curves as *l* increases. Similar behaviours were obtained for the other grounded structures.

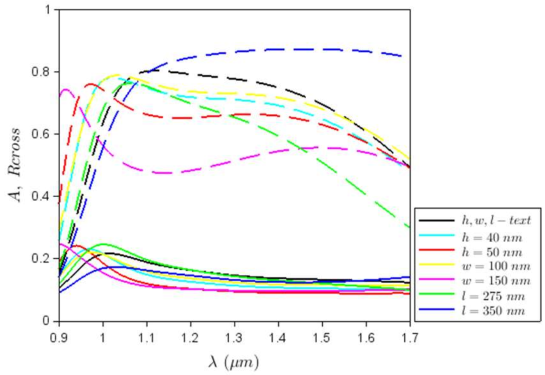

Fig. 8

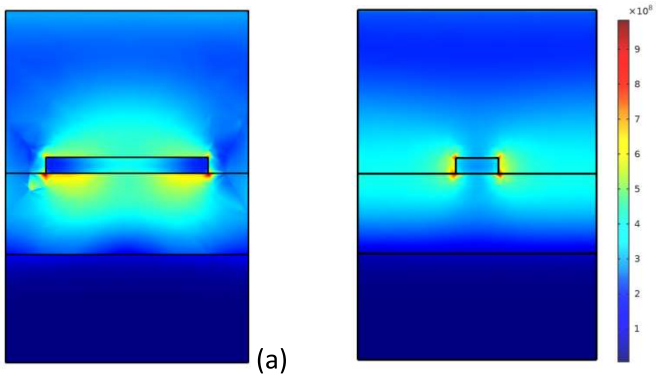

(a) (b) *Fig. 9*

The electric field is localized in the spaces between the metallic meta-atoms, at the top region of the dielectric, and is concentrated at the edges of the meta-atoms. In a way, the electric field can be considered as guided/localized so that the formula for the resonant wavelength in [5] applies. The width of the waveguide is about 300 nm in one direction and about 350 nm in the other direction, which justifies the w_{eff} value chosen above. The fact that the estimated resonant wavelength for *s* = 200 nm is in poorer agreement with that resulting from Fig. 5 can also be understood from Fig. 9, which shows that the electric field is not uniformly spread in the dielectric layer, so that for thicker dielectric layers the effective dimension of the waveguide is smaller than *s*.

- **Advanced multifunctional metalenses**

As discussed previously, both analytical and numerical simulations suggest that the metasurface in Fig. 1, for which the phase difference between cross-polarized fields is controlled by θ, can be used to implement a lens with focal length *f*, which should impart an (ideal) spatially-varying phase $\Delta\varphi_{id} = \varphi(x,y;\lambda) - \varphi(0,0;\lambda) = 2\pi(f - \sqrt{x^2 + y^2 + f^2})/\lambda$ to an incident circularly-polarized optical field. For this purpose, one must divide the wavefront in step-like parts, each of them passing through a metasurface consisting of unit cells in which the meta-atoms have the appropriate rotation angle θ, and look to the cross-polarized component at the output. For example, Fig. 10(a) illustrates the ideal phase distribution of a lens with a focal distance of 10 mm (black line), as well as the step-like approximations when the phase difference imparted by meta-atom rotation between adjacent regions (containing unit cells with the same θ) is 15° (blue line) and 5° (red line), respectively.

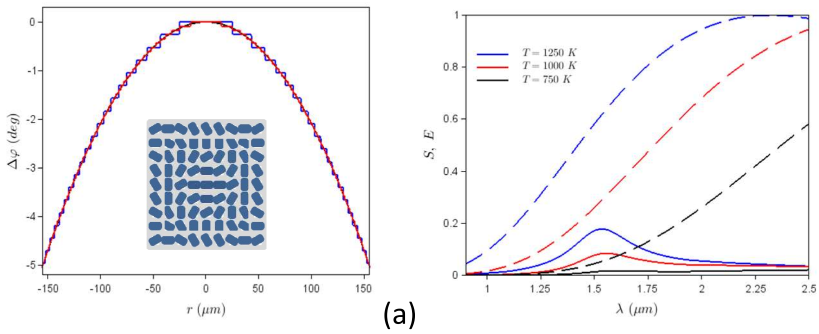

(a) (b)

Fig.10

In the first case 24 regions, of different widths (containing different numbers of unit cells as that in Fig. 1) are needed to cover the whole range of 2π, while in the second case 72 regions are required. In order to estimate the error in phase implementation introduced by the step-like approximation, one can calculate the normalized distance between the ideal and step-like curves as

$\sqrt{\sum_i (\Delta\varphi_{id} - \Delta\varphi_{step})^2 / \sum_i \Delta\varphi_{id}^2}$, where the sum is taken over all edges of all 361 unit cells that form the metalens with the diameter of 300 μm; *r* in Fig. 10(a) denotes the radial coordinate. The obtained value is about 3% for the metastructure with a 15° step in the rotation angle and of only 1% for that with a 5° step. Note however that θ can be rotated continuously between adjacent unit cells such that the error could become even smaller than this value. In addition, in order to not distort the incident wavefront the transmittance/ reflectance of metasurfaces must be the same over the entire lens diameter, condition which has been shown to be fulfilled by both grounded and not grounded investigated structures.

Tuning of the infrared resonant wavelength and absorbance of multifunctional metalenses

In the following there were realised simulations of different cross- and co-polarized reflectances (indices cr and co), of the total reflection (denoted by R), and of the absorbance A of different configurations, investigated in order to identify the optimum one in terms of large and narrow A and Rcr. In the present report there will be presented just a small part.

Therefore, because the structure in Fig. 2, with metallic meta-atoms, does lead to quite wide absorbance curves irrespective of the geometric and material parameters, we have investigated further similar grounded structures but with dielectric meta-atoms, from Al_2O_3, of the same shape (see Fig. 11(a), left), inspired by the results in [12].

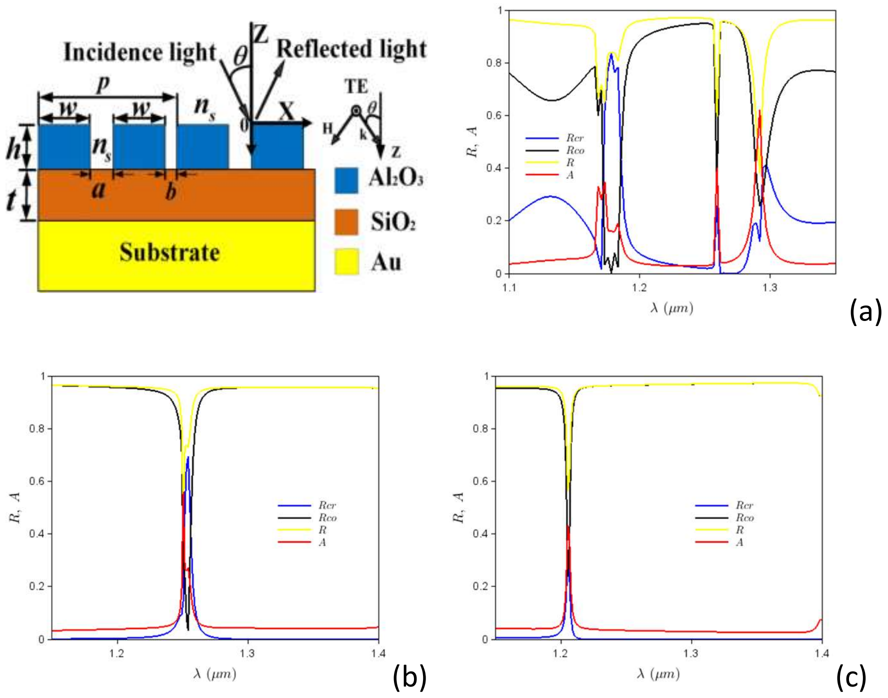

Fig. 11

The corresponding results for Λ = 1000 nm, *w* = 350 nm, *l* = 800 nm, *h* = 950 nm, *a* = 200 nm, *b* = 100 nm, *t* = 1200 nm is illustrated in Fig. 11(a), right. Although *A* and R_{cr} have both high values in very narrow (and multiple) bandwidths, the parameters of the structure, especially *h* and *t*, should be decreased from technological considerations. Therefore, we have investigated different structures. The results for metasurfaces with Λ = 1000 nm, *l* = 600 nm, *h* = 100 nm and (i) *w* = 300 nm, *a* = 250 nm, *b* = 150 nm, *t* = 1200 nm, and (ii) *w* = 200 nm, *a* = 300 nm, *b* = 100 nm, *t* = 500 nm are shown in Figs. 13(b) and (c), respectively. In all cases we can obtain infrared metalenses (with phases controlled by the rotation of meta-atoms), which can at the same time improve considerably the coherence of thermal radiation since *A* is high and very narrow in spectrum.

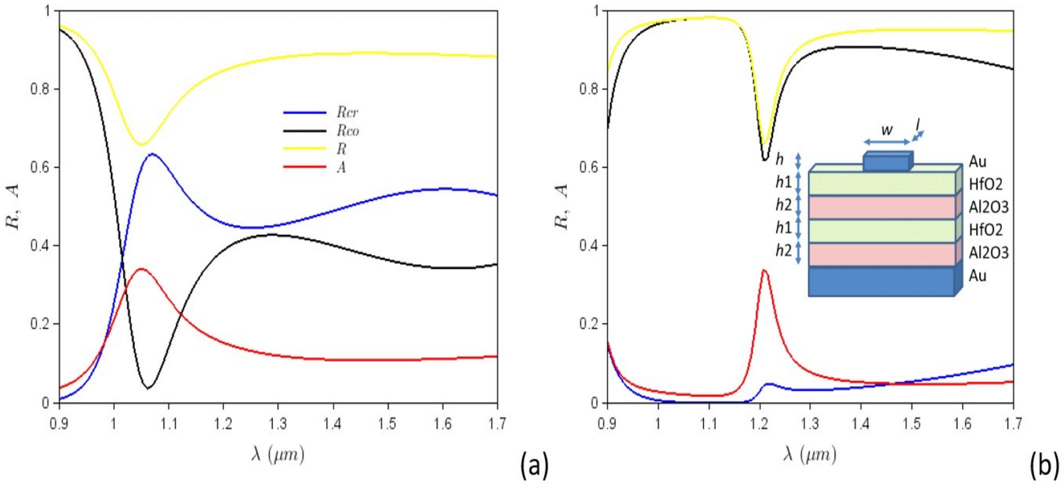

Fig. 12

Whether the results above are satisfactory for the objective of this study, a spectrally extremely narrow absorber and metalens will act only on a correspondingly narrow part of the incident light spectrum. Therefore, in the last part of the investigation we simulated grounded multi-layered dielectric configurations, with metallic meta-atoms. The intent is to find the optimum number of layers/period such that both *A* and R_{cr} have high values with reasonably narrow shapes. Due to the good interfaces and the ease of growing them by atomic layer deposition, we have focused on structures consisting of alternate layers of HfO_2 and Al_2O_3. For the configuration depicted in the inset of Fig. 12(b), with Λ = 400 nm, *w* = 100 nm, *l* = 250 nm, *h* = 30 nm, *h*1 = 50 nm, *h*2 = 40 nm the results are shown in Fig. 12(a), Fig. 12(b) referring to a structure containing 3 periods of HfO_2/Al_2O_3 instead of two. The simulations for the 2-period configuration show an enhanced spectral narrowing of both *A* and R_{cr} with respect to the metasurface having SiO_2 as dielectric, advantage that disappears if the number of periods decreases, as follows from Fig. 12(b).

In conclusion, by modifying the geometric dimensions and constituent materials of the highly anisotropic meta-atoms, one can implement metalenses that control the phase of the cross-polarized field, its reflection coefficient and total absorbance, thus acting also as coherence enhancer for thermal emitters in the near infrared domain. The specific configuration of interest depends on the application and on the available light source.

A2.2 Optimization of the EBL and DRIE processes (IMT-Partner P2):

The first activity connected with the P2 partner is the optimization of the electron beam lithography process that according to our project calendar need it to be done from January till May. The partner has achieved the goal and the deliverable was given in time. At this step, continuing the work from the fires year, the accent was on the optimization of the etching process of the metasurfaces.

To etch the Si metasurfaces, the PlasmaLab100 (Oxford Instruments, UK) fitted with a liquid nitrogen dewar have been used, allowing cryogenic etching processes at temperatures as low as -120 °C.

Table 1: Cryogenic process parameters

ICP power	RF power	Pressure	SF_6 flow	O_2 flow	Table temperature
1200 W	3 W	7,5 mTorr	60 sccm	8 sccm	-115 °C

<u>Process optimization</u> was focused on two aspects: (a) vertical profile of the nanopillars and (b) masking layer. For optimizing the vertical profile of the pillars, the O_2 flow was adjusted to allow near-vertical profiles. During our experimental investigations, we concluded the optimal O_2 flow to be 8 sccm. The plasma parameters used for the cryogenic process are presented in table 1. The etch rate of this proposed process is approximately 28 nm/s. In Fig. 13 are presented the cross sections of pillars etched with optimal and deficient O_2 flow, resulting in a tapered profile.

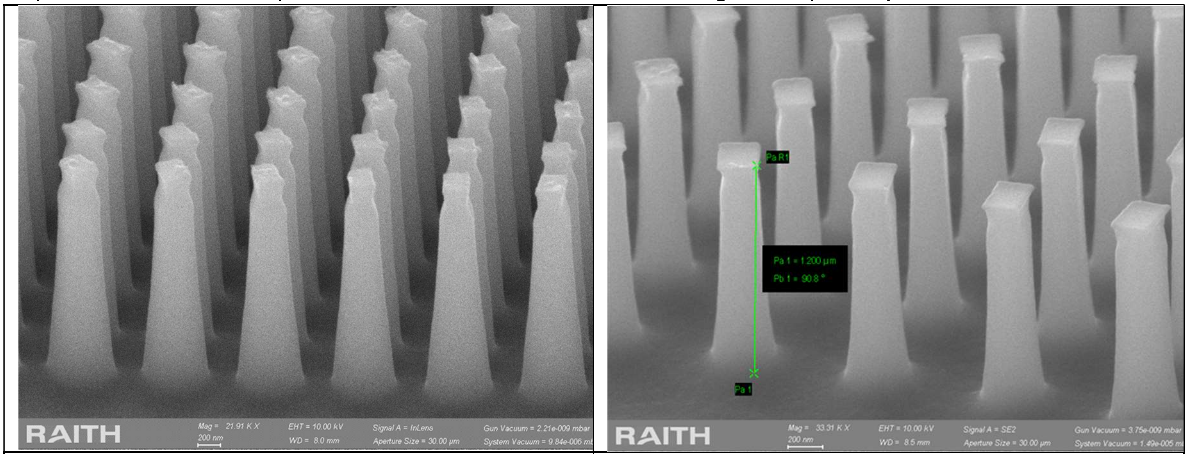

(a) (b)

Fig. 13. Patterned silicon after cryogenic etching process using (a) Al and (b) Ti masking layers

In order to achieve an etch depth of 1200 nm, different thin films were tested as *<u>etching masks</u>*. In this case, we are looking at the selectivity of the etch process, as well as reliable transfer of the designed nano-scale patterns from the mask to the etched structures. Resist masks were excluded due to the shrinkage caused by low substrate temperatures resulting in distorted patterns.

(i) One of the most employed etch masks used in cryogenic etch processes is thermal SiO_2. For this purpose, a thin 100 nm film of SiO_2 was grown on the surface of a Si wafer using a thermal oxidation furnace. The conclusion was that the process is not suitable for optical applications, since the RIE process used for etching SiO_2 results in an increased surface roughness, which is further accentuated during the cryogenic process. As a result, the decision was to use metallic masking layers obtained by a lift-off process.

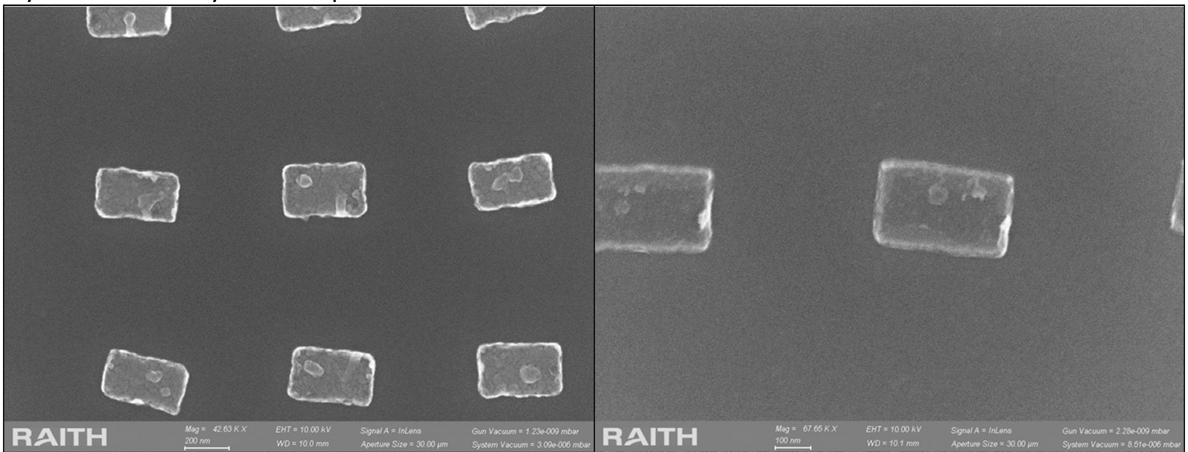

(a) (b)

Fig. 14. E-beam rectangular nanostructures patterned in the: (a) Al and (b) Ti films

(ii) The first metallic mask tested was a thin 50 nm layer of Al. Aluminium was chosen because the potential contamination of the reactor chamber is low due to sputtering by products. After patterning the Al masking layer and etching the Si substrate, we found the structures to have an irregular pattern, most likely due to the large grain size of the metal which prevents accurate transfer of the patterns using a lift-off process.

(iii) By replacing the Al masking layer with a 30 nm thin Ti layer, the pattern of the etched structure was significantly improved resulting in smoother edge lines. In Fig. are the comparative top view SEM images of the patterns transferred in Al and Ti using a lift off process.

A2.3 –Structural Characterization (INCDFM-Project promoter)

Complementary analysis of the EBL metasurfaces fabricated by IMT were realized by the project promoter team. The analysis consists in: scanning electron microscopy, atomic force microscopy, UV-Vis, X-ray measurements and wettability (contact angle measurements).

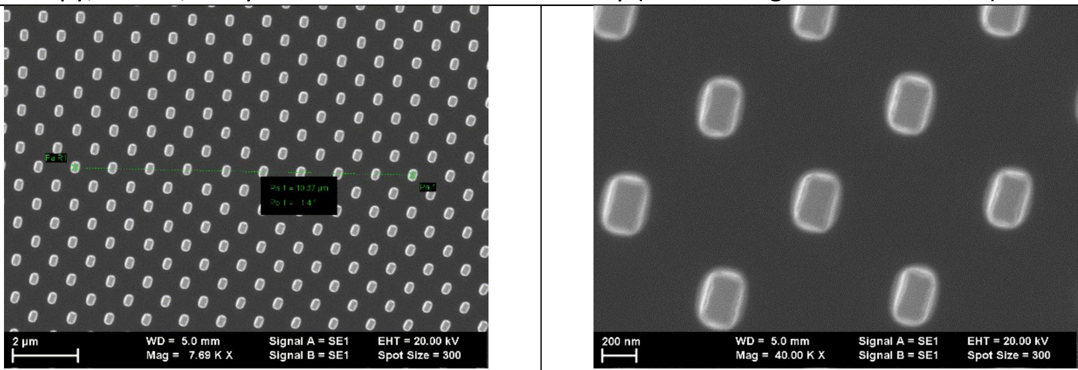

(a) *(b)*

Fig.15 Top view of an optimized EBL metasurface

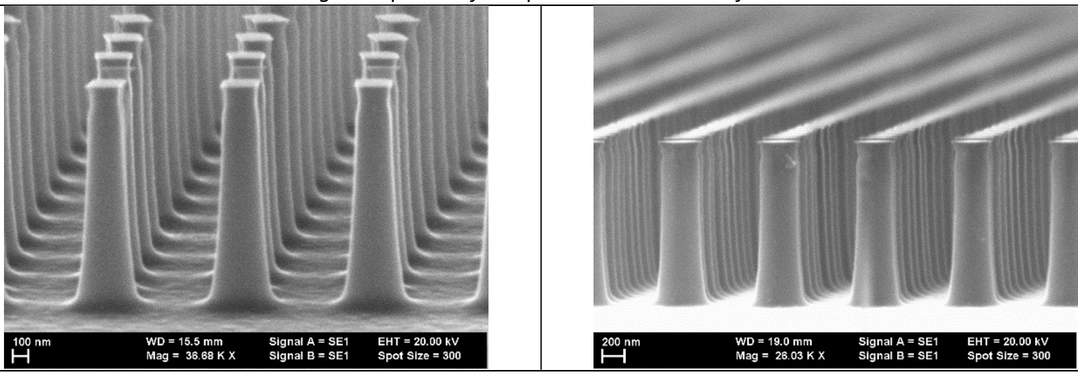

Fig.16 Cross sections of metalenses realized by EBL

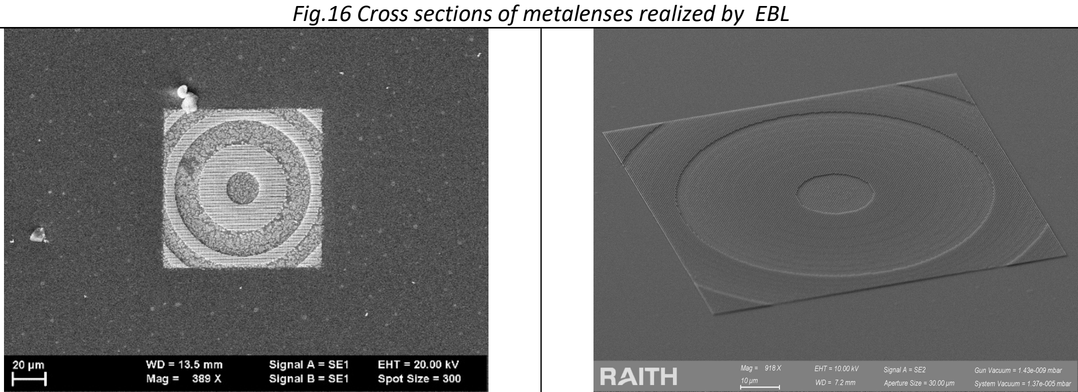

(a) *(b)*

Fig.17 Top view of metalenses: unoptimised (a) - INCDFM SEM, optimized (b)- IMT SEM

Act. 2.4 Lens Characterization set-up (Project Promoter-P1 partner) - the final components have been acquired and with the help of the Skype meetings the home-made set-up have been accomplished on both parts.

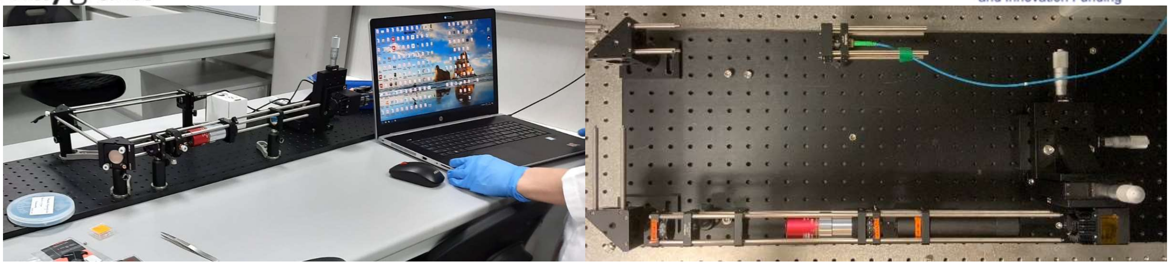

Fig.18 Picture of the set-up realised at the Project Promoter and to the P1 partner

Act. 2.5 Lens and directional emitters obtained by EBL method, characterization (Project Promoter and P1 partner)-

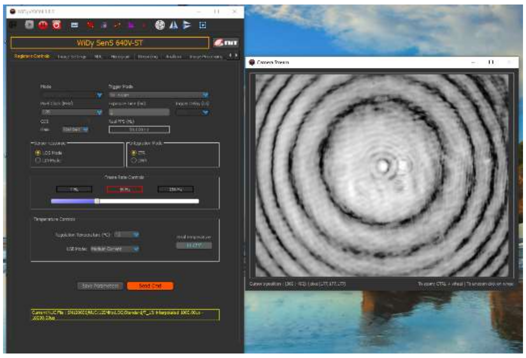

Fig.19. Picture of a focal spot obtained with the Project Promoter set-up

Extensive work on further developing the optical characterization setup at Norwegian partner P1 was done. In particular work was done to verify the efficiency measurements of the metalenses fabricated by P1 for the Optics Express publication in May 2020. Thereafter the Norwegian partner P1 developed a characterization based on thermal sources and filters in order to collect more wavelength datapoints. When used to characterize the metalenses fabricated by IMT-partner P2, good qualitative consistency is observed between them and simulations. Using the thermal source furthermore shows that it is possible to use the metasurfaces fabricating directional sources. It was discovered that some error in the measurement seems to be occurring for wavelengths around 1.31µm. This is possibly explained by the camera sensor being more sensitive in this region than suggested by the datasheet as well as other factors.

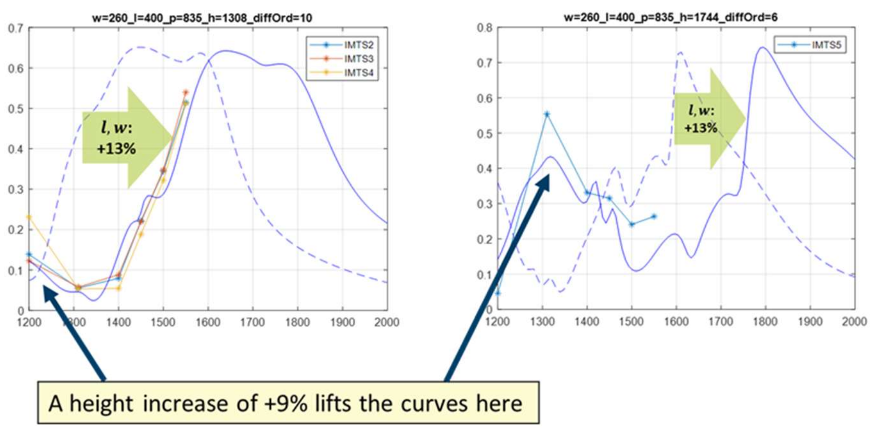

Act. 2.6- Mask Fabrication for UV-NIL – partner P2 (IMT)

The UV-NIL master fabrication was carried out on 4 inches (100) p type silicon wafers, with a resistivity of 5-10 Ω·cm and 525 µm thickness, purchased from Siegert Wafer. The periodic arrays of nanostructured metasurface were performed using both e-beam lithography and cryogenic-deep reactive-ion etching (DRIE) processes. The bottom-up approach employing the evaporation of metal film, followed by the lift-off process was used to build up the nanoscale structures.

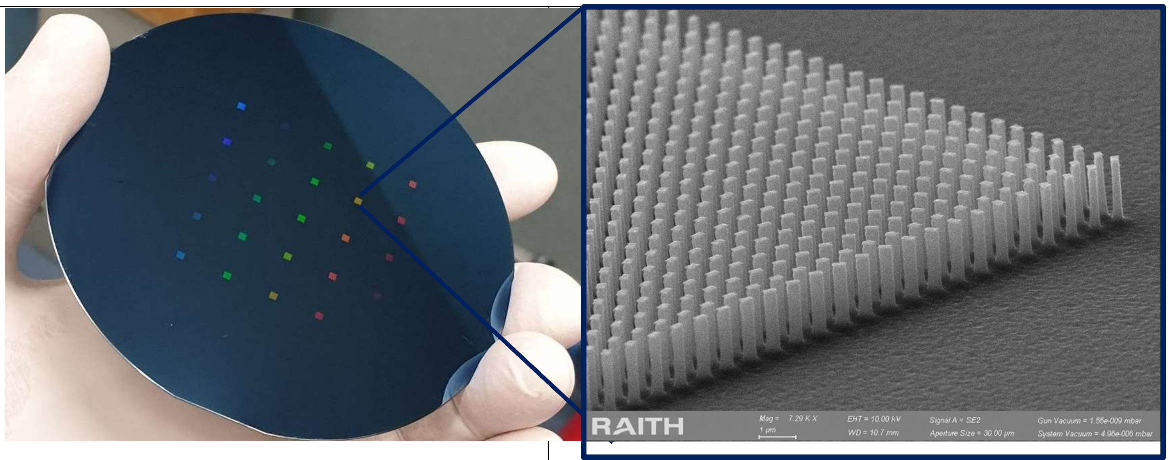

(a)	(b)

Fig.20: 100 mm Si wafer patterned with metasurfaces, and a SEM image with a detail of the metasurface area are we presented

Act.2.7 – UV-NIL metasurface fabrication – Project Promoter

The UV-NIL nanoimprint is a technique that uses transparent hard or soft masks. Thus we need to realise a negative copy of the master provided by the P2 partner on a glass carrier. After a solid documentation two resin polymers were chosen to be used to fabricate the so called "stamps". There were fabricated two types of stamps, using two different polymers: Ormo-Stamp and the new OEM: Shin-Etsu UV-PDMS (KER-4690) both from Micro Resist Technology.

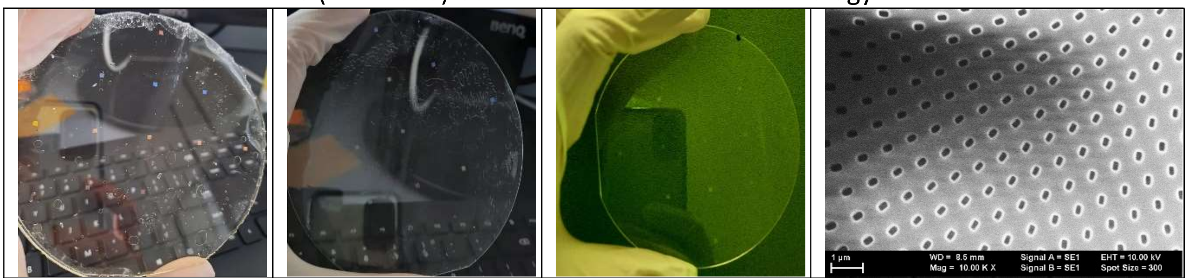

(a)	(b)	(c)	(d)

Fig.21 Different "stamps" made by Ormostamp: (a) first trial by dropcast; (b) first trial by spincast; (c) optimised stamp ; (d) SEM detail of the negative copy of the master imprinted in the polymer

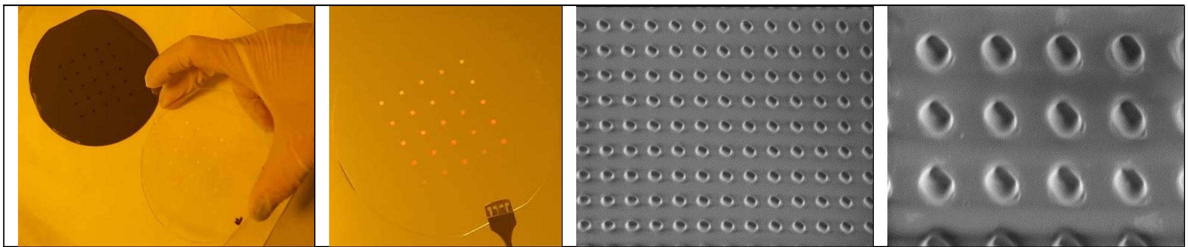

(a)	(b)	(c)	(d)

Fig.22 Different "stamps" made by PDMS by dropcast, (a) first trial with the second master; (b) optimised stamp with the second master ; (c)-(d) SEM detail of the negative copy of the master imprinted in the polymer

The metasurfaces fabrication by UV-NIL can be divided in 2 major steps as follows: (1) the UV-Nanoimprint process which imprints the negative copy of the stamp in a liquid resist sensitive to the

UV-light and (2) cryogenic-DRIE process which gives the final form of the metasuface, etching the silicon wafer.

For the UV-NIL process, the same type of silicon wafers was used, like in the case of the master. The nanoimprint was carried out with an EVG 620 mask aligner.

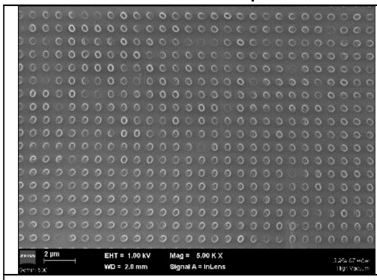

(a)

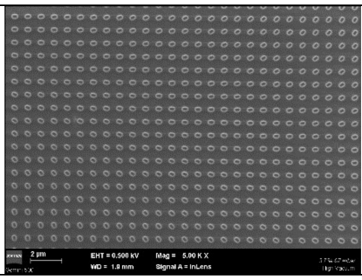

(b)

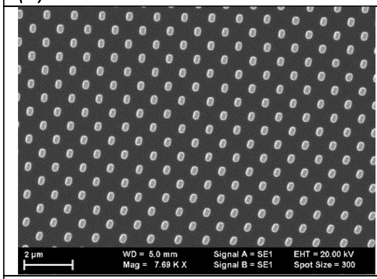

(c)

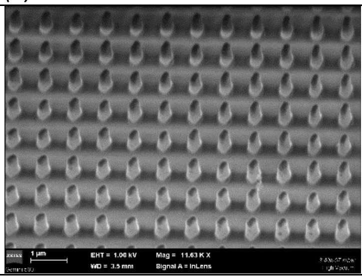

(d)

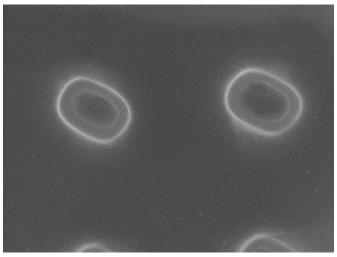

(e)

Fig.23 SEM micrographs of the "metalenses" imprinted in the resist at different contact pressures: (a)50mbar and (b)150mbar; (c) front and (d) side view of an metalens area at 150 mbar pressure; (e) detail of patterns that shows the difference in diameter between bottom and top.

The final step of the metalens fabrication using UV-NIL implies the removal of the residual layer and the dry etching process. This works is done by the **Partner P2**, according with their activity at T3.1 (A 2.7). The mr-NIL-210 residual layer removal was performed using a reactive ion process (RIE) in the Etchlab SI 220 (Sentech Instruments, Germany). The values of this recipe`s parameters included a pressure of 150 mTorr, an ICP power setting of 200 W and 50 sccm O2 flow. The optimal time for the residual layer removal was 50 sec.

Table 2: Cryogenic process parameters

ICP power	RF power	Pressure	SF_6 flow	O_2 flow	Table temperature
1200 W	3 W	7,5 mTorr	60 sccm	8 sccm	-115 °C

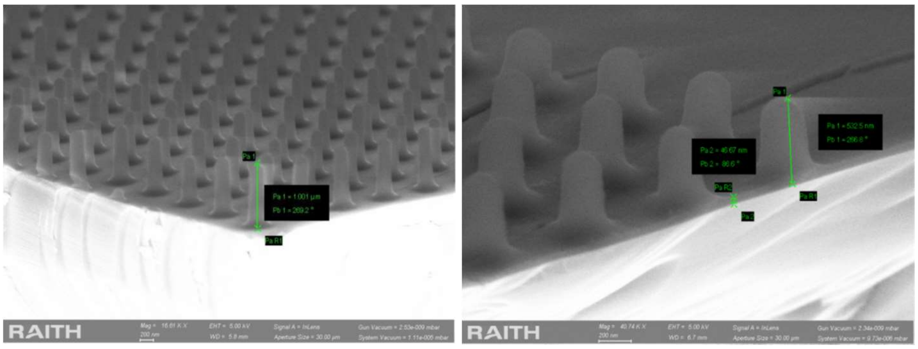

Fig.24 SEM micrographs after residual layer remover

The patterns transfer from the mr-NIL210 resist to silicon was achieved by using the cryogenic process.

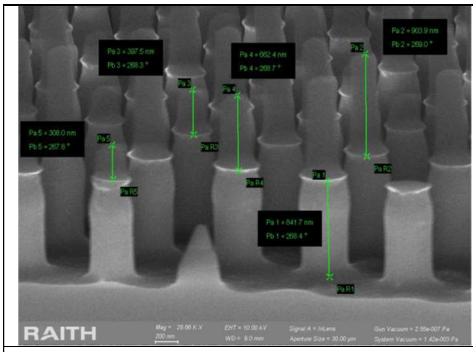

(a)

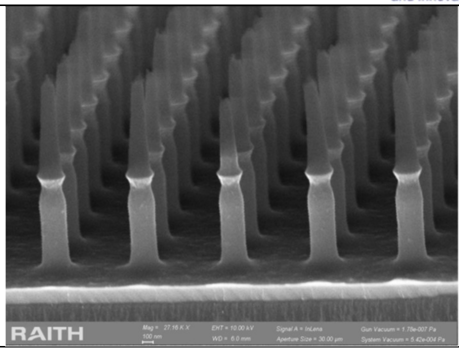

(b)

Fig.25 Side view SEM micrograps of different run etching processes of the metalenses made by UV-NIL

Activity 2.8: Structural Characterization of the UV-NIL metasurfaces (Project Promoter)

Complementary analysis of the NIL metasurfaces fabricated by PP and etched by P2 were realized by the project promoter team. The analysis consists in: scanning electron microscopy, atomic force microscopy, UV-Vis, X-ray measurements and wettability (contact angle measurements).

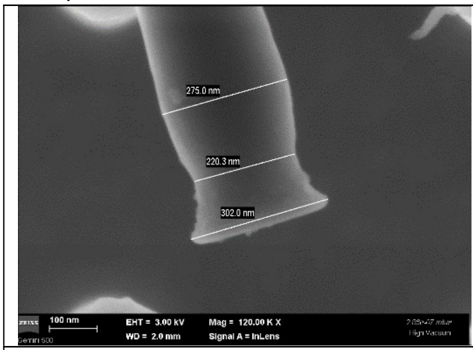

(a)

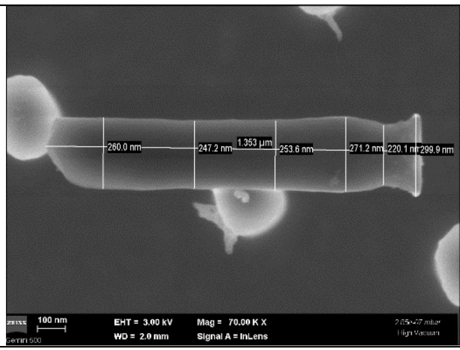

(b)

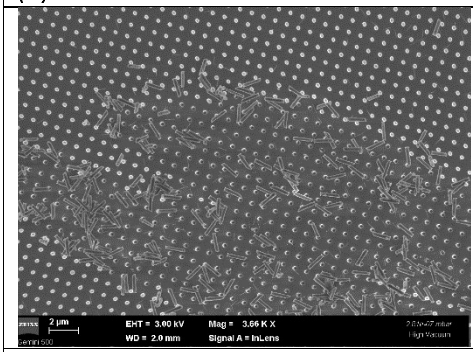

(c)

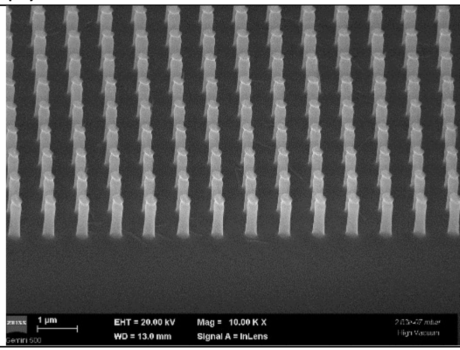

(d)

Fig.26 SEM details of the NIL metasurfaces after completely remove of the mr-NIL 210 mask

The patterns made by UV-NIL are thinner comparing to the ones made by EBL, the difference can be seen more easily in the Fig.27, were are two pictures, one with a metasurface made by EBL and one with a metasurface made by NIL at the same magnification. The rectangular shape is preserved better in the EBL matasurfaces then in the NIL ones, maybe due to the fact that in the mask the pillars and not completely rectangular that implies a negative copy with some with less rectangular patterns.

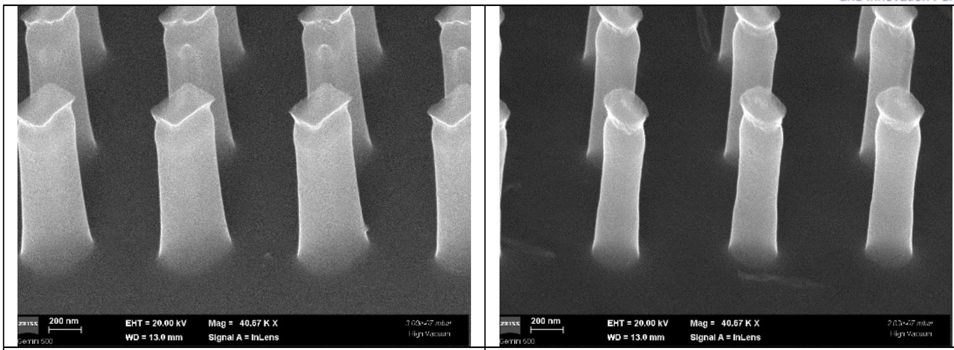

(a) *(b)*

Fig.27 SEM details of a EBL (a) and (NIL) metasurface

Activity 2.9 Optimization of the "UV-NIL" fabrication (PP and P2).

The conclusions after the Promoter and Partner P2 processes are:

(i)The resist films are not uniform – the spinning velocity have to be increased, the both resist dilutions can work;

(ii)The high of the patterns from the "master" has to be less than 1.2µm, between 800-500nm;

(iii)The applied contact pressure has to be above 100mbar in order to have same high for the patterns;

(iV)The residual layer can be completely removed using RIE;

(V) Structures with different etching depth were obtained (starting from 800 till 1.2µm).

Starting from the conclusion– the project promoter already give the P2 partner samples made by deposition of the resist at higher velocity and higher pressure. Attempt to realize the positive stamp starting from master have been done, but the results were not the expected ones due to the fact that the PDMS after 24 hours was not acting like it should act according to the seller. The P2 partner have already provided optimised masters with 800 nm high for the patters.

Dissemination of results

Part of the results presented in this report have been published in the paper *Phase-controlling infrared thermal emitting metasurfaces*, by D. Dragoman, S. Iftimie, A. Radu, in Journal of Optics, https://doi.org/10.1088/2040-8986/abcfd4. Others are the subject of works published in 2021, as will be seen in the "Publications" section of the website, this being one of the reasons that the report of 2020 was made public at the beginning of 2022.

References

[1] S. Tang, T. Cai, H.-X. Xu, Q. He, S. Sun, L. Zhou, Multifunctional metasurfaces based on the "merging" concept and anisotropic single-structure meta-atoms, Appl. Sci. 8, 555, 2018

[2] P.B. Johnson, R.W. Christy, Optical constants of the noble metals, Phys. Rev. B 6, 4370-4379, 1972

[3] W. Ye, Q. Guo, Y. Xiang, D. Fan, S. Zhang, Phenomenological modeling of geometric metasurfaces, Optics Express 24, 7120-7132, 2016

[4] J. Li, B. Yu, S. Shen, Scale law of far-field thermal radiation from plasmonic metasurfaces, Phys. Rev. Lett. 124, 137401, 2020

[5] C. Koechlin, P. Bouchon, F. Pardo, J.-L. Pelouard, R. Haïdar, Analtical description of subwavelength plasmonic MIM resonators and of their combination, Opt. Express 21, 7025-7032, 2013

[6] X. Liu, J. Deng, K. F. Li, Y. Tang, M. Jin, J. Zhou, X. Cheng, W. Liu, G. Li, Optical metasurfaces for designing planar Cassegrain-Schwarzschild objectives**,** Phys. Rev. Appl. 11, 054055, 2019

[7] X. Chen, M. Chen, M.Q. Mehmood, D. Wen, F. Yue, C.-W. Qiu, S. Zhang, Longitudinal multifoci metalens for circularly polarized light, Adv. Optical Mater. 3, 1201-1206, 2015

[8] J.-J. Greffet, M. Nieto-Vesperinas, Field theory for generalized bidirectional reflectivity: derivation of Helmholtz's reciprocity principle and Kirchhoff's law, J. Opt. Soc. Am. A 15, 2735-2744, 1998

[9] D.A.B. Miller, L. Zhu, S. Fan, Universal modal radiation laws for all thermal emitters, PNAS 114, 4336-4341, 2017

[10] D.G. Baranov, Y. Xiao, I.A. Nechepurenko, A. Krasnok, A. Alù, M.A. Kats, Nanophotonic engineering of far-field thermal emitters, Nature Mater. 18, 920-930, 2019

[11] E. Wolf, *Introduction to the Theory of Coherence and Polarization of Light*, Cambridge Univ. Press, Cambridge, U.K., 2007

[12] Y.-L. Liao, Y. Zhao, Ultra-narrowband dielectric metamaterial absorber for sensing based on cavity-coupled phase resonance, Results Phys. 17, 103072 (2020)

[13] Z.-Y. Yang et al., Narrowband Wavelength Selective Thermal Emitters by Confined Tamm Plasmon Polaritons, ACS Photonics 9, 2212–2219 (2017)